# The impact of nuclear shape on the emergence of the neutron dripline

https://doi.org/10.1038/s41586-020-2848-x

Received: 31 December 2019

Accepted: 3 September 2020

Naofumi Tsunoda[1], Takaharu Otsuka[2,3,4,5] ✉, Kazuo Takayanagi[6], Noritaka Shimizu[1], Toshio Suzuki[7,8], Yutaka Utsuno[1,5], Sota Yoshida[9] & Hideki Ueno[3]

Atomic nuclei are composed of a certain number of protons $Z$ and neutrons $N$. A natural question is how large $Z$ and $N$ can be. The study of superheavy elements explores the large $Z$ limit[1,2], and we are still looking for a comprehensive theoretical explanation of the largest possible $N$ for a given $Z$—the existence limit for the neutron-rich isotopes of a given atomic species, known as the neutron dripline[3]. The neutron dripline of oxygen ($Z = 8$) can be understood theoretically as the result of single nucleons filling single-particle orbits confined by a mean potential, and experiments confirm this interpretation. However, recent experiments on heavier elements are at odds with this description. Here we show that the neutron dripline from fluorine ($Z = 9$) to magnesium ($Z = 12$) can be predicted using a mechanism that goes beyond the single-particle picture: as the number of neutrons increases, the nuclear shape assumes an increasingly ellipsoidal deformation, leading to a higher binding energy. The saturation of this effect (when the nucleus cannot be further deformed) yields the neutron dripline: beyond this maximum $N$, the isotope is unbound and further neutrons 'drip' out when added. Our calculations are based on a recently developed effective nucleon–nucleon interaction[4], for which large-scale eigenvalue problems are solved using configuration-interaction simulations. The results obtained show good agreement with experiments, even for excitation energies of low-lying states, up to the nucleus of magnesium-40 (which has 28 neutrons). The proposed mechanism for the formation of the neutron dripline has the potential to stimulate further thinking in the field towards explaining nucleosynthesis with neutron-rich nuclei.

In the accepted simple picture, protons and neutrons in an atomic nucleus are confined by a mean potential, filling single-particle orbits. Like electrons in hydrogen-like atoms, these single-particle orbits have shell structure and magic numbers ($Z$, $N$=2, 8, 20, 28, 50, ....) as conceived by Mayer and Jensen[5,6]. These single-particle orbits for neutrons are displayed schematically in Fig. 1a, b for the example of the magnesium-32 nucleus ($^{32}$Mg; $Z = 12$, $N = 20$). In Fig. 1a, all neutron orbits below $N = 20$ (a magic number) are occupied, forming a neutron closed shell. A closed shell implies a spherical shape in general (Fig. 1c). However, if single-particle orbits are only partially filled, the picture is altered. If the nucleons are scattered, giving rise to longer mutual distances (Fig. 1d), a weaker binding is induced because of the short-range attractive nuclear force. On the other hand, if the nucleons are closely configured, forming an ellipsoid (Fig. 1e), mutual distances between the nucleons become shorter, resulting in stronger binding due to the nuclear force. Thus, an ellipsoidal shape[7–9] can arise.

For the example of $^{32}$Mg, if neutrons are excited across $N = 20$ magic gap (Fig. 1b), orbits below and those above $N = 20$ are both partially filled. A deformed shape can then arise. The binding energy is increased by the deformation. If this effect is large enough that its energy gain overcomes the energy needed to promote neutrons across the magic gap, this state is low in energy, and is called an 'intruder' (Fig. 1b, e). If the intruder becomes the ground state as in $^{32}$Mg, it is called an inversion[10–14], a breaking of Mayer–Jensen's magic scheme (Fig. 1a, c).

Here we present a theoretical description of magic number, shell, shape and dripline properties of nuclei with $Z = 9$–$12$. Experimentally known neutron driplines are reproduced for $Z = 9$ and 10. Likewise, experimental excitation energies of low-lying states are reproduced, confirming the validity of this calculation. In isotopes of $Z = 10$–$12$, as $N$ increases from 20, the ellipsoidal shape deformation remains large, which results in strong binding. This effect, however, terminates at a certain $N$, and the isotope chain reaches the dripline. This mechanism is in contrast to the traditional scenario in which, near driplines, the last neutrons occupy loosely bound single-particle states[15–18].

## Nuclear chart, exotic nuclei and dripline

The nuclear analogue of the periodic table is the Segrè chart (or nuclear chart). Figure 2a shows a part of it for $Z = 1$–$16$. Each square in this chart

---

[1]Center for Nuclear Study, The University of Tokyo, Tokyo, Japan. [2]Department of Physics, The University of Tokyo, Tokyo, Japan. [3]RIKEN Nishina Center, Saitama, Japan. [4]KU Leuven, Instituut voor Kern- en Stralingsfysica, Leuven, Belgium. [5]Advanced Science Research Center, Japan Atomic Energy Agency, Ibaraki, Japan. [6]Department of Physics, Sophia University, Tokyo, Japan. [7]Department of Physics, College of Humanities and Sciences, Nihon University, Tokyo, Japan. [8]National Astronomical Observatory of Japan, Tokyo, Japan. [9]Liberal and General Education Center, Institute for Promotion of Higher Academic Education, Utsunomiya University, Tochigi, Japan. ✉e-mail: otsuka@phys.s.u-tokyo.ac.jp

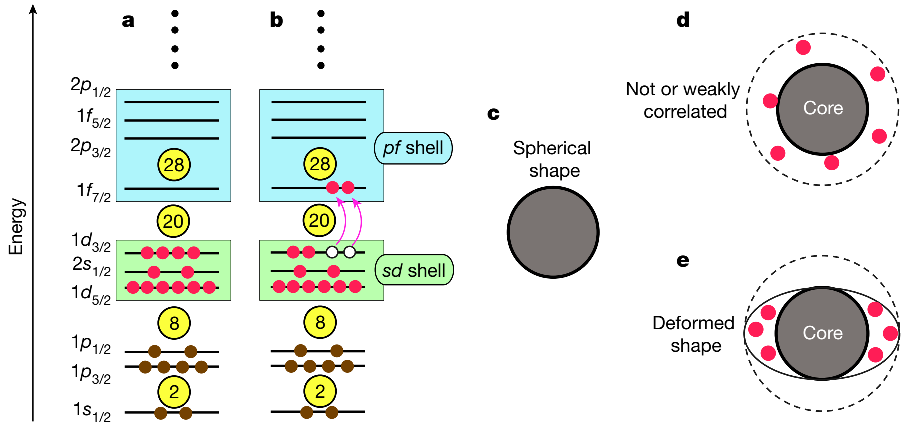

**Fig. 1 | Schematic illustrations of shell structure and nuclear shape.** **a**, **b**, Shell structure of neutrons for $^{32}$Mg. The numbers in circles with yellow highlight denote Mayer–Jensen's magic numbers[5,6]—2, 8, 20, 28, ... The *sd* shell is indicated by the green background; the *pf* shell is indicated by the blue background. All orbits below the magic number $N = 8$ are occupied by neutrons (brown circles), forming the inert core. The vertical dots at the top imply higher orbits. **a**, The lowest orbits are occupied (filling scheme): $N$ is 20 for $^{32}$Mg, which is a magic number; all orbits in the *sd* shell are then occupied by neutrons (red circles) forming the $N = 20$ closed shell. **b**, As in **a**, but two neutrons are excited from the *sd* shell (holes shown by white circles) to the *pf* shell (red circles), as shown by pink arrows. **c**–**e**, Spherical and ellipsoidal shapes. **c**, The shape is spherical, for instance, for the ground state with $N$ and $Z$ being magic numbers. **d**, A typical configuration of valence nucleons without substantial correlations among them. **e**, An ellipsoidal deformed shape formed by closely configured valence nucleons with strong correlations.

corresponds to an individual nucleus with specific values of $Z$ and $N$. Black squares imply stable nuclei, which have infinite or long enough lifetimes. The element name and the mass number, $A = Z + N$, are indicated. Stable nuclei constitute most of the matter on the Earth. Orange squares indicate the remaining nuclei, called exotic nuclei. Exotic nuclei can exist for finite, usually rather short, lifetimes, because they decay into other nuclei through radioactive decay, primarily through $\beta$ decay[1], eventually reaching stable nuclei after sequential decays. Thus, exotic nuclei are literally 'exotic' in nature. They are, however, produced constantly in the Universe as intermediate products in stellar nucleosynthesis or in nuclear reactors.

The chain of isotopes (that is, the horizontal span in $N$ for each $Z$) in the Segrè chart ends at the neutron dripline. Its location on the chart, as well as its underlying mechanism, is one of the most intriguing problems of nuclear physics at present, and is our focus here. Figure 2a indicates that as $Z$ increases, the dripline moves farther right in the Segrè chart; more protons in a nucleus means that the nucleus can hold more neutrons[1]. We also note that some nuclei with odd $N$ do not exist near the dripline. The dripline has been established experimentally up to $Z = 10$; see below.

Stable and exotic nuclei are called bound nuclei, in the sense that protons and neutrons are put together by nuclear forces indefinitely or until radioactive decays change them to other nuclei. Open squares in Fig. 2a mean unbound systems, which are usually called unbound 'nuclei' regardless of their instability against neutron (or proton) emissions, and can be observed, for instance, as resonance-like peaks in the emission spectra. By identifying relevant unbound nuclei such as those indicated by open squares in Fig. 2a, one can experimentally confirm the dripline.

## Configuration-interaction calculation up to driplines

Here we study the stable and exotic nuclei in the isotopic chains of fluorine (F, $Z = 9$), neon (Ne, $Z = 10$), sodium (Na, $Z = 11$) and magnesium (Mg, $Z = 12$). Wide ranges of $N$ are covered. Particle–hole excitations across the $N = 20$ magic gap, an example of which is shown by dark pink arrows in Fig. 1b, are crucial in many of these nuclei. Other particle–hole combinations should be included, and multiple particle–hole excitations can occur. Consequently, two major shells below and above the magic number 20 (the *sd* and *pf* shells, respectively, as shown in Fig. 1a, b) must be explicitly treated in the theoretical calculation. We take the $^{16}$O closed shell, where all single-particle orbits below the magic number 8 are fully occupied (brown circles in Fig. 1a, b). The *sd* and *pf* shells provide single-particle states where active (or valence) nucleons can move around, interacting with each other. This interaction has been derived[4], via the extended Kuo–Krenciglowa (EKK) method[19–21], from the fundamental chiral-effective-field-theory ($\chi$EFT) interaction by Machleidt and Entem[22] stemming from quantum chromodynamics (Methods). The derivation of an effective $NN$ interaction like this is not trivial. For example, relevant earlier methods may encounter difficulties of divergence, once both the *sd* and *pf* shells are included[21]. The EKK method resolves this difficulty. The contributions from three-nucleon forces (3NF) are further included into this effective $NN$ interaction[4,23], where the 3NF represents effects of virtual excitations to the $\Delta$ particle, that is, the Fujita–Miyazawa force[24] (Methods). The present effective interaction, called EEdf1, is thus constructed[4]. The Schrödinger equation is solved for this interaction using a configuration-interaction-type calculation, called the shell-model calculation in nuclear physics (Methods). We note that in traditional shell-model calculations, some parts of the $NN$ interaction are usually adjusted by using experimental data (see this review[13]). In addition, ab initio shell-model-type approaches have worked well recently, but some difficulties appear when going through $N = 20$; see, for example, refs. [25,26].

The nine nuclei with $Z = 10$–$12$ and $N = 20$–$22$ are often referred to collectively as the island of inversion[12], named after their intruder ground states (Methods). A number of earlier works have been reported on many nuclei in and near the island of inversion (see reviews[13,27]). More recently, those nuclei have also been described by the EEdf1 interaction[4,27–32]. Here we extend the application of the EEdf1 calculation towards driplines. Figure 3 displays such results for the excitation energies of the $2_1^+$ and $4_1^+$ states in even-$N$ Ne and Mg isotopes. We observe a good agreement with experiment, including those (Ne with $N = 22$ and Mg with $N = 24$, 26 and 28) measured after the derivation of the EEdf1 interaction. Low-lying $2_1^+$ and $4_1^+$ energy levels are usually good indicators of substantial ellipsoidal deformation, and this is the case for $N \geq 20$ in Fig. 3.

We note that configuration-interaction calculations to solve the present eigenvalue problem cannot be performed for $N = 24$–$30$ within the traditional computational method, that is, the diagonalization of a Hamiltonian matrix, because the dimensions of the matrix exceed the

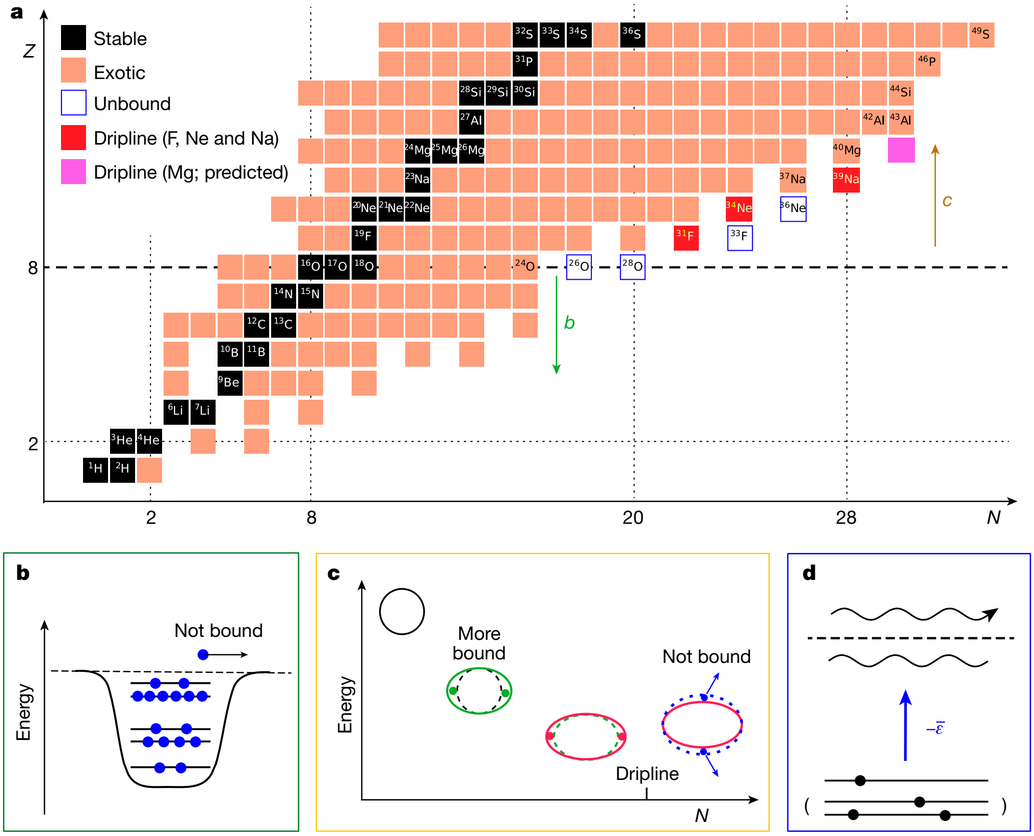

**Fig. 2 | The Segrè (nuclear) chart (from hydrogen up to sulfur) and schematic pictures for the dripline mechanisms. a**, Part of the Segrè chart, where individual atomic nuclei are plotted as squares for their $Z$ and $N$. The name of the element and its mass number ($A = Z + N$) are shown in some squares. Mayer–Jensen's magic numbers are denoted along the axes. The thin dotted lines indicate those magic numbers in the chart, whereas the dashed line indicates the $Z = 8$ magic number. The black squares indicate stable nuclei, and the orange ones indicate exotic nuclei observed experimentally so far. The red squares are driplines for F, Ne and (probably) Na isotopes, while the pink square is the present prediction for Mg isotopes. The blue-outlined squares indicate experimentally known unbound nuclei relevant to this work. The green arrow labelled *b* suggests the region in the chart where the dripline mechanism shown in panel **b** is considered to be applicable; the brown arrow labelled *c* suggests the region in the chart where the dripline mechanism shown in panel **c** is considered to be applicable. **b**, Traditional picture of dripline mechanism based on the filling of single-particle orbits from the bottom. **c**, New dripline mechanism based on shape evolution and the resulting change of the binding energy. **d**, The energy needed to move one of the neutrons in the ground state (brackets) to a loosely bound or continuum single-particle states (wavy lines). The upper wavy line with arrowhead implies a state in the continuum.

current limit[33], which is $10^{11}$. We employ the Monte Carlo shell model, which enables us to solve this eigenvalue problem to a good approximation by means of selected important basis vectors for a given many-body state[34,35] (see recent applications[36–38] and Methods).

## Ground-state energy, dripline and magic number

We calculate the ground-state energies relative to that of the $^{16}O$ nucleus and compare them to experimental data (Fig. 4). A good agreement is seen in each panel. Although the *NN* interaction was derived as described above, the single-particle energies with respect to the $^{16}O$ inert core were fitted as free parameters for the original EEdf1 Hamiltonian[4] (Methods). In principle, the single-particle energies can be derived, but more studies are needed to achieve an accuracy comparable to that of the effective *NN* interaction. The validity of these fitted values has been confirmed by comparison to a number of experimental data not only of energy levels but also of electromagnetic properties or spectroscopic factors[4,28–32]. Although the derivation of the effective *NN* interaction does exhibit a certain ab initio aspect, this fit prevents us from calling the present calculation fully ab initio.

We now calculate the ground-state energies of the four isotopic chains up to their driplines. The driplines obtained by the original EEdf1 calculation differ somewhat from recent experimental ones for F and Ne isotopes[39]. To retain the advantage of the successful application of the original EEdf1 calculation, we simply shift all the single-particle energies by the same amount, $\Delta\varepsilon$. This shift changes neither excitation energies nor wavefunctions, but varies the ground-state energies.

As shown in the Methods, $\Delta\varepsilon = 0.82$ MeV appears to be appropriate, and so we use it in this work. Figure 4 shows the ground-state energies for each chain of isotopes: as $N$ starts to increase, the ground-state energy first comes down, and reaches a minimum point. Beyond this minimum point, the ground-state energy becomes higher, meaning that a certain energy can be released by breaking this nucleus into a lighter one and some fragment(s) including neutron(s); this nucleus is unbound. The minimum points (red arrows) in Fig. 4 correspond to the driplines. Figure 4 displays only isotopes with even values of $N$. This is because near the dripline, isotopes with odd values of $N$ show higher ground-state energies, and what is relevant to the dripline is the comparison between even-$N$ isotopes.

Figure 4 indicates that the present calculation reproduces observed driplines[39] at $^{31}F$ and $^{34}Ne$ as well as the probable candidate at $^{39}Na$, and predicts the dripline at $^{42}Mg$ (Fig. 2a, Methods and Extended Data Fig. 1). Earlier dripline works show similarities and differences to this work: for example, a mean-field calculation[3] predicted driplines at $N = 24 \pm 2$ and $32 \pm 2$ for Ne and Mg isotopes, respectively, while an empirical approach[40] predicted driplines at $^{29}F$, $^{34}Ne$, $^{37}Na$ and $^{40}Mg$.

Figure 2b exhibits a schematic picture of an underlying mechanism of the dripline: neutrons fill single-particle orbits in the mean potential,

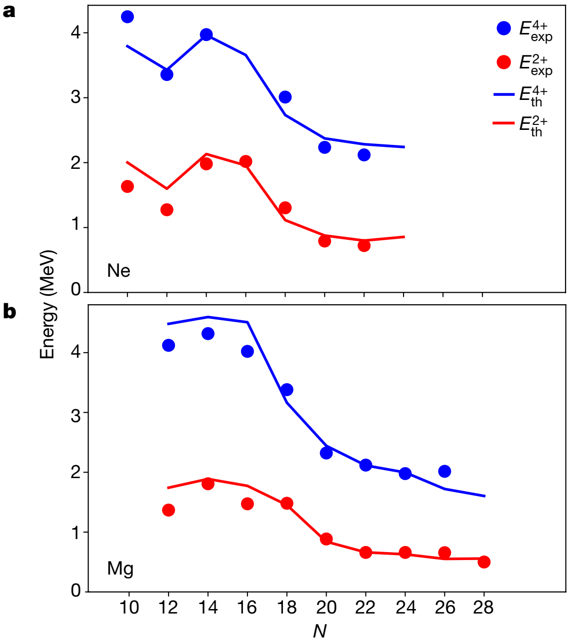

**Fig. 3 | Systematic variations of the $2_1^+$ and $4_1^+$ energy levels of Ne and Mg isotopes, as functions of N. a**, Ne; **b**, Mg. The results of the present configuration-interaction calculation with the EEdf1 interaction (lines) are compared to experimental data (symbols)[31]. Data are from the National Nuclear Data Center's 'Evaluated Nuclear Structure Data File' (http://www.nndc.bnl.gov/ensdf/).

but the last neutron cannot occupy any bound orbit. As this neutron must go away, the nucleus is unbound. This scenario basically represents the situation of the oxygen isotopes. The two highest bound orbits, the $1d_{5/2}$ (lower) and $2s_{1/2}$ (higher) orbits (Fig. 1a, b), are fully occupied. The next orbit is the $1d_{3/2}$ orbit. In oxygen isotopes, there is a new magic number $N = 16$, with a sizeable gap between the $1d_{3/2}$ and $2s_{1/2}$ orbits (see a review[27]) partly due to the tensor force[41]. The $1d_{3/2}$ orbit is located high in energy, because of this gap, at positive energy or the continuum. This feature remains unchanged in oxygen isotopes due to 3NF (ref. [23]). In fact, $^{26}$O and $^{28}$O have been known experimentally to be unbound (open squares in Fig. 2a), locating the dripline at the $^{24}$O nucleus[42,43]. Thus, the magic number/shell structure and the dripline can be linked directly. As the mean potential is mainly due to the proton–neutron interaction, the mean potential for neutrons is shallower for smaller $Z$, because of fewer protons. Neutron orbits are then lifted up in energy, and the highest orbit can be pushed up into the continuum. Thus, the neutron dripline moves to smaller $N$ value as $Z$ decreases, although the actual mechanism can be more complex. If the last bound single-particle state of neutrons is loosely bound, an outward tunnelling may occur, ending up with a neutron halo, that is, an extremely extended neutron density distribution[15–18]. The coupling of such loosely bound states to continuum states is of current interest, leading to an open system[44].

## Another dripline mechanism and nuclear shapes

We next discuss how the dripline is determined in neon and magnesium isotopes. We decompose the effective $NN$ interaction, $v_{NN}$, into three components according to their effects (not their origins):

$$v_{NN} = v_{\rm mono} + v_{\rm pair} + v_{\rm rest} \qquad (1)$$

where $v_{\rm mono}$, $v_{\rm pair}$ and $v_{\rm rest}$ denote the monopole, pairing and rest interactions, respectively. This decomposition is made uniquely for a given $v_{NN}$ (Methods). We start with a simple explanation of them. We take two

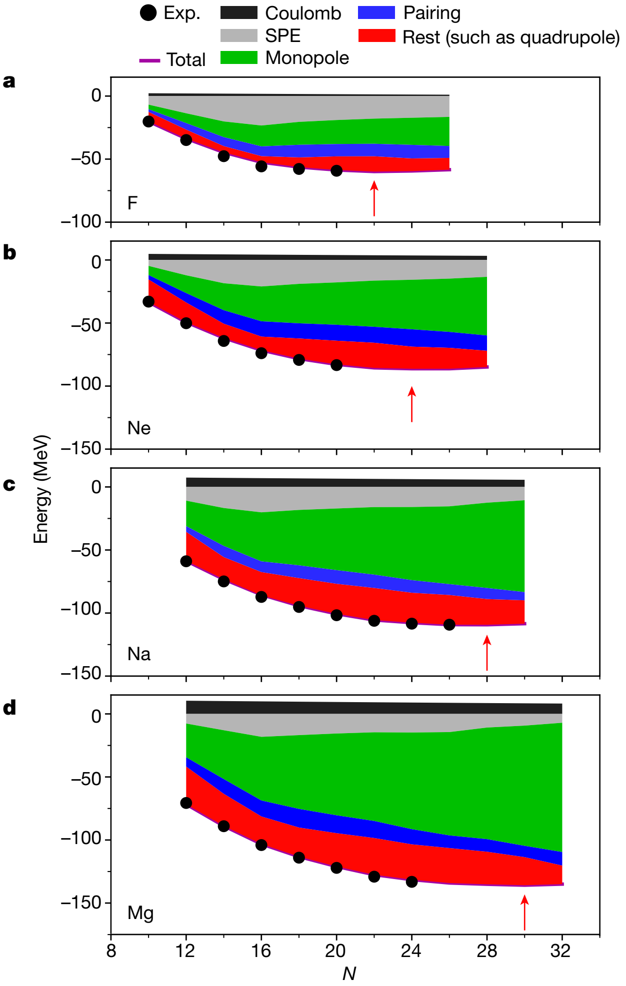

**Fig. 4 | Ground-state energies of even-$N$ isotopes of F, Ne, Na and Mg, relative to the $^{16}$O value.** Coloured segments exhibit decompositions into various effects from the monopole (green), pairing (blue) and rest (such as quadrupole) (red) components of the effective nucleon–nucleon interaction as well as those from Coulomb interaction (black) and single-particle energies (labelled SPE; grey). The monopole effect grows steadily as a function of $N$ in all cases; the rest effect is also substantial but varies in more complex ways. The experimental values are indicated by closed black circles: data are from the National Nuclear Data Center's 'Evaluated Nuclear Structure Data File' (http://www.nndc.bnl.gov/ensdf/). The theoretical driplines indicated by red arrows are the same as the experimental ones for F and Ne isotopes, and probably also for Na isotopes. The dripline of Mg isotopes is not known experimentally.

single-particle orbits $j$ and $j'$. The monopole interaction represents an average effect between a nucleon in $j$ and another in $j'$ for $v_{NN}$ (see a review[27]). The average is taken over all possible quantum states of these two nucleons. The effect of the monopole interaction is given by the product of the occupation numbers of the orbit $j$ and that in $j'$. It resembles the bond between two interacting objects.

The pairing interaction in atomic nuclei induces nucleon-pair correlations in the angular momentum space in the same way as the BCS (Bardeen–Cooper–Schrieffer) pairing in linear momentum space in condensed matter. The pairing interaction is then extracted from $v_{NN}$ after the removal of the monopole component, as a component acting on two neutrons (or two protons) in the same orbits but in opposite directions, coupled to $J^\pi = 0^+$ (where $J$ is total angular momentum and $\pi$ is parity). This interaction moves such a pair from an orbit to another, keeping $J^\pi = 0^+$, and is one of the major sources of binding energy.

The 'rest' interaction collectively implies all other terms after extracting the monopole and the pairing components from $v_{NN}$. Although the

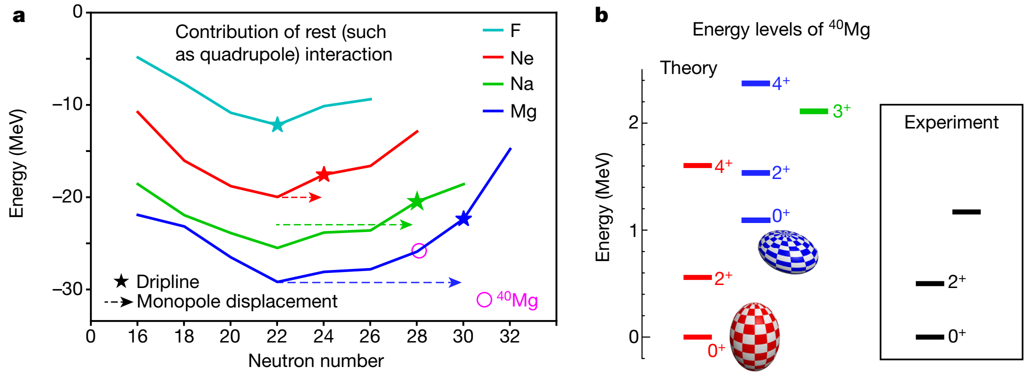

**Fig. 5 | Contribution of the rest (such as quadrupole) component of the effective nucleon–nucleon interaction and the energy level scheme of $^{40}$Mg. a**, The contribution to the ground states as functions of $N$ for even-$N$ isotopes of F, Ne, Na and Mg. Star symbols denote driplines (Fig. 4). Dashed arrows indicate the displacements mainly due to the single-particle-energy plus monopole (that is, combined monopole) effects (Fig. 4). The $^{40}$Mg nucleus is indicated by a circle. **b**, On the left, theoretical energy levels below 2.5 MeV are shown, including the prolate ground (red) and triaxial side (blue) rotational bands. The shapes of the bands are shown by illustrative symbols. On the right, the experimental levels are shown[47].

rest interaction consists of many terms with various effects, the effect most relevant to this work is the generation of more binding energies for stronger ellipsoidal (or quadrupole) deformation, illustrated in Fig. 1e. Because other effects may also provide some binding energies, the contribution of the rest interaction is referred to as ‘rest (such as quadrupole)’ in Figs. 4 and 5a as well as in the text.

Figure 4a–d displays the contributions of these three terms, as well as the contribution of the Coulomb interaction evaluated as in the previous work[4]. All these contributions are shown relative to the values for the $^{16}$O core. The effects of the single-particle energy are negative in Fig. 4, and the positive Coulomb effects are cancelled by part of the single-particle energy effects.

The monopole interaction effectively changes the single-particle energies (see a review[27]). It is therefore natural to combine the effect of the single-particle energy (grey in Fig. 4) and that of the monopole interaction (green), and to call it the combined-monopole effect, including the Coulomb effect as well. This combined effect is seen as the lower edge of the green area in Fig. 4. If this edge comes down as $N$ is increased, added neutrons are bound as far as the combined-monopole effect is concerned. For Ne isotopes, the lower edge of the green area comes down to $N=30$, even beyond the dripline. Similar trends are seen for Na and Mg isotopes. This means that an added neutron gains some binding energy from the combined-monopole effect even beyond the dripline. So there must be another mechanism to push the driplines back to the right places. The pairing interaction is basically irrelevant to this, because its effect is rather stable as a function of $N$ around the driplines.

Figure 5a displays the contribution of the rest (such as quadrupole) interaction. We focus on the Mg case first: as $N$ increases from 16, this contribution becomes larger in magnitude but comes to the turning point at $N=22$. Although it does not change much until $N=26$, it rises rapidly for $N>26$. Note that a similar trend is expected for the quadrupole deformation, which can be quantified, for example, by electric quadrupole properties. In fact, a consistent enhancement of their values is seen in the present calculation, exhibiting agreement with experiment for lighter isotopes[4] while heavier ones are experimental challenges. The ground-state energy is lowered until the turning point at $N=30$ (Fig. 4d). Thus, the rest (such as quadrupole) contribution and the ground-state energy show different turning points. We point out that the combined-monopole effect changes, as a function of $N$, almost linearly as −2.4 MeV per $N$ in the range $N=22$–32. The rest (such as quadrupole) contribution, however, exhibits a different pattern, like a parabola. In going from $N=30$ to 32, it becomes too weak to be compensated by the monopole effect, lifting the $N=32$ ground state above the $N=30$ ground state in energy. Thus, the Mg dripline is placed at $N=30$. Neither magic number $N=20$ or $N=28$ characterizes the nuclei being discussed: for example, the neutron $1d_{3/2}$ orbit (Fig. 1a) remains only about half-filled still in the $^{42}$Mg ground state, implying that the intruder nature persists beyond the island of inversion[12,45]. The parabolic behaviours[14] as a function of $N$ in Fig. 5a are stretched both ways far beyond $N=20$ and 28, whereas if these magic numbers dominated the structure of these nuclei, the parabolas would end there.

Figure 2c displays this situation intuitively: the variation of the shape and ground-state energy are depicted as a function of $N$, starting from a spherical shape at a higher energy. By adding neutrons, the ellipsoidal deformation evolves, giving the nucleus additional binding energy (second object from left in Fig. 2c). Because such deformation is a realization of the Jahn–Teller effect[46], special superpositions of single-particle states are needed to enlarge the deformation. We note that besides the superpositions in the $pf$ shell, there can be other superpositions by neutron holes (Fig. 1b). The deformed ground-state wavefunction contains some of these superpositions (second object from left in Fig. 2c). At a certain value of $N$, all available superpositions are in the wavefunction, implying that this extra binding effect is saturated, marking a maximum (third object from left in Fig. 2c). After this point, additional neutrons weaken the deformation, for instance, yielding triaxial shapes (on the far right in Fig. 2c).

On top of this effect, as explained above for Mg isotopes, there is a displacement between the minimum point of the rest (such as quadrupole) effect and the dripline, mainly due to the combined-monopole effect (arrows in Fig. 5a). If this monopole effect is weaker, the displacement becomes smaller. In fact, there is no such effect for F isotopes (see the top part of Fig. 5a). For Ne isotopes, the monopole effect changes by approximately −0.9 MeV per $N$ in the range $N=20$–28, producing a smaller displacement of $\Delta N=2$, as compared to $\Delta N=6$ (8) for Na (Mg) isotopes (Fig. 5a). We note that the pairing interaction is included in the present calculation but does not change the basic trend. Thus, for the isotopes being discussed, the dripline is given by the saturation of the rest (such as quadrupole) effect combined with the present outward displacement. Because the present effective $NN$ interaction has been derived from the basic nuclear forces (see Methods for their possible variations), both effects are expected to be robust, providing a visible example of the dripline mechanism.

It is then of particular importance to examine the present approach by comparing with experimental data near the dripline. For this question, we present the energy levels of $^{40}$Mg, for which experimental data became available very recently[47]. Despite a plausible claim about the incapability of “any currently published calculations”[47], Fig. 5b exhibits a nice agreement for the energy levels of $^{40}$Mg. In this case, the Monte

Carlo Shell Model (MCSM) calculation yields a rotational band built on the ground state with a prolate shape (red), and another rotational band with a triaxial shape at very low excitation energy (blue). This agreement seems to suggest the validity of the present approach.

We now comment on the traditional view that loosely bound neutrons characteristic of dripline nuclei may show notable coupling to continuum states, referred to as "open system"[44]. When the gain of the combined-monopole effect with one more neutron is denoted as $\bar{\epsilon}$, $-\bar{\epsilon}$ represents, as a rough estimate, the energy needed to promote a neutron from the ground state to a loosely bound state, assuming that all effects except for the combined-monopole effect are unchanged (Fig. 2d). In the case of Mg isotopes, the open-system scheme may show up, in this estimate, with excitation energies around $-\bar{\epsilon} \approx 2.4$ MeV, apart from other effects. As $\bar{\epsilon}$ is much smaller for F isotopes, this coupling can occur at lower excitation energy. It is of great interest to see such variations. If *N* is an odd integer, the pairing and rest (such as quadrupole) effects are weaker. This is one of the reasons why only even-*N* isotopes appear near driplines, and the open system may be found in low-lying states with odd *N*, for example[48].

## Prospects

Here we have described a mechanism for the dripline of atomic nuclei, to which both the variation of the shape deformation and the combined-monopole effect contribute. Although this mechanism is not very sensitive to details, the agreement with a variety of experimental data and the ab initio nature of the effective *NN* interaction enhance the reality of the mechanism. The patterns of the monopole and rest effects in Fig. 4 have been observed in other regions of the Segrè chart[27], and their combination, naturally and robustly, gives us the present dripline mechanism, in which the EEdf1 interaction provides their precise magnitudes. It is remarkable that the driplines of F, Ne and probably Na isotopes are described within a single framework of EEdf1 interaction, despite the large structural changes observed. The excited states are described also, including the recent data for $^{40}$Mg. As a general outcome, this work proposes two dripline mechanisms: one with a single-particle nature and the other with shape deformation (the collective mode), as shown in Fig. 2b, c, respectively. These two mechanisms are complementary, and may appear alternatively as *Z* increases. For instance, the mechanism in Fig. 2b may return for the magic number $Z \approx 20$. The interplay of single-particle versus collective aspects has been studied in many facets of nuclear structure[49,50], and is now shown to be crucial also to the dripline. Including intermediate situations, it is of great interest where and how these two mechanisms arise as *Z* changes as well as how one can observe them experimentally, for example, by measuring ellipsoidal deformation of the nuclei towards driplines. The relation between fission and the present mechanism is of interest as the limiting case of the dripline in heavy nuclei.

## Online content

Any methods, additional references, Nature Research reporting summaries, source data, extended data, supplementary information, acknowledgements, peer review information; details of author contributions and competing interests; and statements of data and code availability are available at https://doi.org/10.1038/s41586-020-2848-x.

1. Indelicato, P. & Karpov, A. Sizing up atoms. *Nature* **498**, 40–41 (2013).
2. Nazarewicz, W. The limits of nuclear mass and charge. *Nat. Phys*. **14**, 537–541 (2018).
3. Erler, J. et al. The limits of the nuclear landscape. *Nature* **486**, 509–512 (2012).
4. Tsunoda, N. et al. Exotic neutron-rich medium-mass nuclei with realistic nuclear forces. *Phys. Rev. C* **95**, 021304(R) (2017).
5. Goeppert Mayer, M. On closed shells in nuclei. II. *Phys. Rev*. **75**, 1969 (1949).
6. Haxel, O., Jensen, J. H. D. & Suess, H. E. On the "magic numbers" in nuclear structure. *Phys. Rev*. **75**, 1766 (1949).
7. Rainwater, J. Nuclear energy level argument for a spheroidal nuclear model. *Phys. Rev*. **79**, 432 (1950).
8. Bohr, A. & Mottelson, B. R. *Nuclear Structure* Vol. II (Benjamin, 1975).
9. Casten, R. F. *Nuclear Structure From A Simple Perspective* (Oxford Univ. Press, 2000).
10. Thibault, C. et al. Direct measurement of the masses of $^{11}$Li and $^{26-32}$Na with an on-line mass spectrometer. *Phys. Rev. C* **12**, 644–657 (1975).
11. Guillemaud-Mueller, D. et al. *β*-Decay schemes of very neutron-rich sodium isotopes and their descendants. *Nucl. Phys. A* **426**, 37–76 (1984).
12. Warburton, E. K., Becker, J. A. & Brown, B. A. Mass systematics for A = 29–44 nuclei: the deformed A ~ 32 region. *Phys. Rev. C* **41**, 1147 (1990).
13. Caurier, E., Martínez-Pinedo, G., Nowacki, F., Poves, A. & Zuker, A. P. The shell model as a unified view of nuclear structure. *Rev. Mod. Phys*. **77**, 427–488 (2005).
14. Heyde, K. & Wood, J. L. Shape coexistence in atomic nuclei. *Rev. Mod. Phys*. **83**, 1467 (2011).
15. Tanihata, I. et al. Measurements of interaction cross sections and nuclear radii in the light *p*-shell region. *Phys. Rev. Lett*. **55**, 2676–2679 (1985).
16. Hansen, P. G. & Jonson, B. The neutron halo of extremely neutron-rich nuclei. *Europhys. Lett*. **4**, 409 (1987).
17. Gade, A. & Glasmacher, T. In-beam nuclear spectroscopy of bound states with fast exotic ion beams. *Prog. Part. Nucl. Phys*. **60**, 161–224 (2008).
18. Nakamura, T., Sakurai, T. & Watanabe, H. Exotic nuclei explored at in-flight separators. *Prog. Part. Nucl. Phys*. **97**, 53–122 (2017).
19. Takayanagi, K. Effective interaction in non-degenerate model space. *Nucl. Phys. A* **852**, 61–81 (2011).
20. Takayanagi, K. Effective Hamiltonian in the extended Krenciglowa-Kuo method. *Nucl. Phys. A* **864**, 91–112 (2011).
21. Tsunoda, N., Takayanagi, K., Hjorth-Jensen, M. & Otsuka, T. Multi-shell effective interactions. *Phys. Rev. C* **89**, 024313 (2014).
22. Machleidt, R. & Entem, D. R. Chiral effective field theory and nuclear forces. *Phys. Rep*. **503**, 1 (2011).
23. Otsuka, T., Suzuki, T., Holt, J. A., Schwenk, A. & Akaishi, Y. Three-body forces and the limit of oxygen isotopes. *Phys. Rev. Lett*. **105**, 032501 (2010).
24. Fujita, J. & Miyazawa, H. Pion theory of three-body forces. *Prog. Theor. Phys*. **17**, 360 (1957).
25. Stroberg, S. R. et al. Nucleus-dependent valence-space approach to nuclear structure. *Phys. Rev. Lett*. **118**, 032502 (2017).
26. Simonis, J., Stroberg, S. R., Hebeler, K., Holt, J. D. & Schwenk, A. Saturation with chiral interactions and consequences for finite nuclei. *Phys. Rev. C* **96**, 014303 (2017).
27. Otsuka, T., Gade, A., Sorlin, O., Suzuki, T. & Utsuno, Y. Evolution of shell structure in exotic nuclei. *Rev. Mod. Phys*. **92**, 015002 (2020).
28. Loelius, C. et al. Enhanced electric dipole strength for the weakly bound states in $^{27}$Ne. *Phys. Rev. Lett*. **121**, 262501 (2018).
29. Fernández-Domínguez, B. et al. Re-examining the transition into the N = 20 island of inversion: structure of $^{30}$Mg. *Phys. Lett. B* **779**, 124 (2018).
30. Xu, Z. Y. et al. Nuclear moments of the low-lying isomeric $1^+$ state of $^{34}$Al: Investigation on the neutron 1*p*1*h* excitation across *N* = 20 in the island of inversion. *Phys. Lett. B* **782**, 619 (2018).
31. Murray, I. et al. Spectroscopy of strongly deformed $^{32}$Ne by proton knockout reactions. *Phys. Rev. C* **99**, 011302(R) (2019).
32. Nishibata, H. et al. Structure of $^{31}$Mg: shape coexistence revealed by *β*-*γ* spectroscopy with spin-polarized $^{31}$Na. *Phys. Rev. C* **99**, 024322 (2019).
33. Shimizu, N., Mizusaki, T., Utsuno, Y. & Tsunoda, Y. Thick-restart block Lanczos method for large-scale shell-model calculations. *Comput. Phys. Commun*. **244**, 372–384 (2019).
34. Otsuka, T., Honma, M., Mizusaki, T., Shimizu, N. & Utsuno, Y. Monte Carlo shell model for atomic nuclei. *Prog. Part. Nucl. Phys*. **47**, 319–400 (2001).
35. Shimizu, N. et al. New-generation Monte Carlo shell model for the K computer era. *Prog. Theor. Exp. Phys*. **2012**, 01A205 (2012).
36. Marsh, B. A. et al. Characterization of the shape-starggering effect in mercury nuclei. *Nat. Phys*. **14**, 1163–1167 (2018).
37. Ichikawa, Y. et al. Interplay between nuclear shell evolution and shape deformation revealed by the magnetic moment of $^{75}$Cu. *Nat. Phys*. **15**, 321–325 (2019).
38. Taniuchi, R. et al. $^{78}$Ni revealed as a doubly magic stronghold against nuclear deformation. *Nature* **569**, 53–58 (2019).
39. Ahn, D. S. et al. Location of the neutron dripline at fluorine and neon. *Phys. Rev. Lett*. **123**, 212501 (2019).
40. Koura, H. et al. Nuclidic mass formula on a spherical basis with an improved even-odd term. *Prog. Theor. Phys*. **113**, 305–325 (2005).
41. Otsuka, T., Suzuki, T., Fujimoto, R., Grawe, H. & Akaishi, Y. Evolution of the nuclear shells due to the tensor force. *Phys. Rev. Lett*. **95**, 232502 (2005).
42. Fauerbach, M. et al. New search for $^{26}$O. *Phys. Rev. C* **53**, 647–651 (1996).
43. Sakurai, H. et al. Evidence for particle stability of $^{31}$F and particle instability of $^{25}$N and $^{28}$O. *Phys. Lett. B* **448**, 180–184 (1999).
44. Dobaczewski, J., Michel, N., Nazarewicz, W., Płoszajczak, M. & Rotureau, J. Shell structure of exotic nuclei. *Prog. Part. Nucl. Phys*. **59**, 432–445 (2007).
45. Caurier, E., Nowacki, F. & Poves, A. Merging of the islands of inversion at *N* = 20 and *N* = 28. *Phys. Rev. C* **90**, 014302 (2014).
46. Jahn, H. A. & Teller, E. Stability of polyatomic molecules in degenerate electronic states. I—Orbital degeneracy. *Proc. R. Soc. Lond. A* **161**, 220 (1937).
47. Crawford, H. L. et al. First spectroscopy of the near drip-line nucleus $^{40}$Mg. *Phys. Rev. Lett*. **122**, 052501 (2019).
48. Nakamura, T. et al. Deformation-driven *p*-wave halos at the drip line: $^{31}$Ne. *Phys. Rev. Lett*. **112**, 142501 (2014).
49. Bohr, A. & Mottelson, B. R. *Nuclear Structure* Vol. I (Benjamin, 1969).
50. Otsuka, T., Tsunoda, Y., Abe, T., Shimizu, N. & Van Duppen, P. Underlying structure of collective bands and self-organization in quantum systems. *Phys. Rev. Lett*. **123**, 222502 (2019).

## Methods

### EKK method

The EEdf1 interaction is derived by using the EKK method, which is explained here. The EKK method is a version of many-body perturbation theory. The many-body perturbation theory stands for a group of the methods for deriving the effective interaction designed for a given model space (for example, the *sd* or *sd-pf* shells), starting from the nuclear force in vacuum[51]. The Kuo–Krenciglowa (KK) method[52] is also one of the many-body perturbation theories, and has been used conventionally and successfully for this purpose[51]. One cannot, however, utilize the KK method for a model space composed of more than one major shell, owing to the divergence problem of the perturbative expansion.

In the framework of many-body perturbation theory, including the EKK and KK methods, a bare nuclear force in vacuum is renormalized to an effective interaction for the designated model space. The renormalization is materialized by perturbative techniques to take in the effects of the virtual excitation to the outside of the model space. This is the reason for the divergence in the KK method, because the naive treatment of the energy denominator leads to a divergence if the model space comprises more than one major shell. Unfortunately, this has been a fundamental issue of many-body perturbation theories.

To describe many exotic nuclei, the model space composed of more than one major shell (for example, the *sd-pf* shell) is essential but one cannot access, using the KK method, this interesting and fruitful region of the Segrè chart. The EKK method has overcome this difficulty by re-summing the perturbative series so that one can avoid the divergence. The re-summation is performed with a formula similar to the Taylor expansion but in the operator form. One can avoid the divergence by choosing an appropriate value of the 'origin' of the expansion, without changing the result, as long as the summation of the series converges. The detailed derivation and explanation of the EKK method are shown in refs. [19–21].

### EEdf1 interaction and its single-particle energies

The first application of the EKK method was carried out for the study of the nuclei around the island of inversion, as described in ref. [4]. We outline here how the effective interaction for the shell model calculation was constructed.

The $\chi$EFT interaction proposed by Entem and Machleidt[22,53] was taken with $\Lambda = 500$ MeV, as the nuclear force in vacuum mentioned above, up to the next-to-next-to-next-to-leading-order (N3LO) in the $\chi$EFT. It was then renormalized by the $V_{\mathrm{low}k}$ approach[54,55] with a cutoff of $\Lambda_{V\mathrm{low}k} = 2.0\ \mathrm{fm}^{-1}$, in order to obtain a low-momentum interaction decoupled from high-momentum phenomena. This treatment helps to generally improve the convergence of the many-body perturbation theory calculation, which is in this case, the EKK method. The EKK method was then adopted in order to obtain the effective *NN* interaction for the *sd-pf* shell, by including the so-called $\hat{Q}$-box, which incorporates unfolded effects coming from the outside of the model space[51], up to the third order and its folded diagrams. As the single-particle basis vectors, the eigenfunctions of the three-dimensional harmonic oscillator potential were taken as usual. On top of this, the contributions from the Fujita–Miyazawa 3NF were added in the form of the effective *NN* interaction. The Fujita–Miyazawa force[24] represents effects of the virtual excitation from a nucleon to a $\Delta$ baryon by pion-exchange processes. It has been discussed and included in many works, for instance[56,57]. While the 3NFs may contain other terms, the Fujita–Miyazawa force is considered to produce dominant contributions to binding energies, as shown, for instance, in ref. [23]. Furthermore, its major and important roles have recently been clarified also from the viewpoint of the $\chi$EFT interaction[58]. The other terms are still under discussions with variations of their strength parameters among different $\chi$EFT approaches, and their effects are expected to be small with respect to the present issues. We thus retained the Fujita–Miyazawa force in evaluating contributions from the 3NFs, but other 3NFs will be discussed later.

The effective *NN* interaction for the *sd-pf* shell was thus constructed, and was named the EEdf1 interaction. There are seven single-particle orbits in the *sd-pf* shell. Their single-particle energies are determined by the fit, as stated in the main text. We note that only the single-particle energies are fitted and the interaction between valence nucleons in the *sd-pf* shell is derived as mentioned above. Because of the isospin symmetry, a proton orbit has the same energy as the corresponding neutron orbit except for the Coulomb contribution, which is assumed to be equal to all proton orbits (for a given nucleus) as usual. The values of the seven single-particle energies were determined so as to reproduce observables such as the ground-state energies of $N < 20$, the $2_1^+$ level of $^{30}$Ne, $^{32}$Mg, $^{34}$Si, and the excitation energies of several states of $^{31}$Mg. The fit was not like a $\chi^2$-fit but was done so as to reproduce basic patterns of these observables. The single-particle energies of the $2p_{1/2}$ and $1f_{5/2}$ orbits are constrained by the GXPF1 values[59], as described also in ref. [4]. We note that no structure data of neutron-rich exotic nuclei with $N > 20$ were used in this fit.

The EEdf1 interaction and the single-particle energies attached to it were thus constructed. It has been extensively applied to a variety of cases: many experimental data other than those used for the fit are described well, as one can find not only in Figs. 3, 4, but also in the results shown in refs. [4,27–32].

As stated in the main text, the single-particle energies need to be refined from the original EEdf1 values. In the present work, we shift them by the same amount, $\Delta\varepsilon$. We first investigate, for each isotopic chain, which nucleus becomes the dripline as a function of $\Delta\varepsilon$. As shown in Extended Data Fig. 1, the original values of the single-particle energies ($\Delta\varepsilon = 0$) are too low, and the calculated dripline appears too far from the experimentally observed location in the Segrè chart. By increasing the $\Delta\varepsilon$ value, the dripline is shifted to smaller $N$ values, that is, to lighter isotopes (Extended Data Fig. 1). The driplines were assigned experimentally to $^{31}$F and $^{34}$Ne very recently[39], suggesting the range $\Delta\varepsilon = 0.82$–$1.17$ MeV. Regarding the chain of Na isotopes, a preliminary report indicates, with one event, that $^{39}$Na is bound[39]. The nucleus $^{37}$Na is known to be bound[60]. If the dripline is on $^{39}$Na, $\Delta\varepsilon = 0.82$–$0.87$ MeV is obtained (dark pink belt in Extended Data Fig. 1). As it is very unlikely from empirical systematics that $^{41}$Na is bound, we exclude this possibility. We thus adopt $\Delta\varepsilon = 0.82$ MeV, the lower boundary of the range. This range, 0.050 MeV, is the uncertainty of this study and limits, for instance, the precision of the one-neutron separation energy; it is too small to be visible in Extended Data Fig. 1. The $^{40}$Mg isotope is known to be bound[61], and the predicted dripline of Mg isotopes is $^{42}$Mg (Extended Data Fig. 1).

### Uncertainty quantification

The comparisons to experimental data stated in the previous section reinforce the validity of the EEdf1 interaction for the present study. While this kind of comparison is a standard way to ensure the validity of a given theoretical scheme, another approach, called the uncertainty quantification, has been investigated in recent years[3,62–64]. By using this approach, different treatments of a common nuclear force in vacuum can be compared in order to see the variable range of the outcome. In the present work, we have discussed the uncertainty due to the range of the shift $\Delta\varepsilon$, giving rise to limited precision of the neutron separation energies. This affects only ground-state energies.

Recently, a variety of ab initio effective *NN* interactions have been proposed[25,26,65–76]; different choices of the nuclear force in the free space and varying recipes of its renormalization lead to different effective *NN* interactions. To reinforce our findings including the dripline mechanism, therefore, it is desirable to perform the uncertainty quantification analysis by adopting other effective *NN* interactions into the present scheme. Although such a full-scale calculation is ideal, it is at present not feasible because of limited computational resources. We therefore explore how results are varied by changing the interactions.

The present work uses the cutoff parameter $\Lambda_{V\mathrm{low}k} = 2.0\ \mathrm{fm}^{-1}$ in the $V_{\mathrm{low}k}$ calculation[54,55]. We vary $\Lambda_{V\mathrm{low}k}$ from $2.0\ \mathrm{fm}^{-1}$ to $1.8\ \mathrm{fm}^{-1}$ and $2.2\ \mathrm{fm}^{-1}$. Note that $\Lambda_{V\mathrm{low}k} = 1.8\ \mathrm{fm}^{-1}$, $2.0\ \mathrm{fm}^{-1}$ and $2.2\ \mathrm{fm}^{-1}$ were used in earlier works, such as ref. [77]. The $\chi$EFT N3LO *NN* interaction mentioned above[22,53] is renormalized with these three values of $\Lambda_{V\mathrm{low}k}$, and is further transformed, by the EKK method, into the effective *NN* interaction for configuration-interaction calculations. The expectation values of such effective *NN* interactions are calculated with respect to the ground-state wavefunctions obtained in the work described in the main text. Although the third-order $\hat{Q}$-boxes were included in the EKK calculation for the results shown in the main text, this comparison with different values of $\Lambda_{V\mathrm{low}k}$ is made at the second-order $\hat{Q}$-box, for the sake of simplicity. The Ne and Mg isotopes with $N \geq 16$ are considered up to near their driplines. The comparison shows rather weak dependence on $\Lambda_{V\mathrm{low}k}$. The expectation values appear to be similar for the three different values of $\Lambda_{V\mathrm{low}k}$, for a given isotope in both Ne and Mg isotopic chains (Extended Data Fig. 2). The change of this expectation value from $^{26}$Ne to $^{38}$Ne is more directly related to the driplines, and is shown to be insensitive to the $\Lambda_{V\mathrm{low}k}$ value: it is −57.16 MeV, −57.57 MeV and −58.27 MeV, respectively, for $\Lambda_{V\mathrm{low}k} = 1.8\ \mathrm{fm}^{-1}$, $2.0\ \mathrm{fm}^{-1}$ and $2.2\ \mathrm{fm}^{-1}$. The deviation is $\lesssim 1\%$. The Mg isotopes show a similar insensitivity: the corresponding changes from $^{28}$Mg to $^{44}$Mg are −102.62 MeV, −102.10 MeV and −101.49 MeV. The third-order $\hat{Q}$-box results are slightly above these second-order $\hat{Q}$-box results (Extended Data Fig. 2). This can be a hint of good convergence as a function of the $\hat{Q}$-box order, and enhances the validity of the present comparison.

We also found, in the analysis stated above, that the monopole, pairing and rest (such as quadrupole) components in equation (1) depict similarly weak dependences on $\Lambda_{V\mathrm{low}k}$. The expectation values of the rest (such as quadrupole) term by the second-order $\hat{Q}$-box calculation provide an example of the insensitivity to the $\Lambda_{V\mathrm{low}k}$ value (Extended Data Fig. 3), including the location of its maximum magnitude ($N = 22$, that is, $^{32}$Ne and $^{34}$Mg), which has exactly the same location as in Fig. 5. This indicates that the second-order results already carry essential properties of the structure evolution. Such similarities between the second- and third-order results are seen also for the monopole and pairing terms.

Another variation is investigated for the 3NF. The Fujita–Miyazawa 3NF, which we adopt here, does not contain the so-called $c_\mathrm{D}$ and $c_\mathrm{E}$ contact terms[78,79]. Although there are various options of 3NF that include these terms, we use the following two frequently used 3NFs: one given by Hebeler et al.[77] (option of 2.0/2.0 (EM $c_i$ values) for $V_{\mathrm{low}k}$) and the other by Gazit et al.[80]. We obtain effective *NN* interactions from these 3NFs first by deriving density-dependent *NN* interactions from them[81], and then by having the density dependence integrated out with the normal density. Similarly to the cutoff dependences discussed above, we calculate the expectation values of such effective *NN* interactions with respect to the ground-state wavefunctions of the Ne and Mg isotopes with $N \geq 16$ up to near the driplines (Extended Data Fig. 4). The resultant expectation values derived from the 3NF of Gazit et al.[80] show quite good agreement with the values obtained from the currently used Fujita–Mitazawa 3NF. We note that $c_\mathrm{D} = 0.83$ and $c_\mathrm{E} = -0.052$ are adopted besides the standard $c_1 c_3 c_4$ term[80]. In fact, the expectation value of the Fujita–Mitazawa (Gazit et al.) 3NF is 11.2 (12.3) MeV for $^{28}$Mg and 46.4 (49.2) MeV for $^{44}$Mg. This close relation indicates that the Fujita–Mitazawa 3NF adopted in this work may be, especially in practice, not too far from the 3NFs used in other approaches, providing us with an indication of the robustness of the present dripline mechanism. The 3NFs of Hebeler et al.[77], where $c_\mathrm{D} \approx 1.6$–$1.7$ and $c_\mathrm{E} \approx -0.1$, show some systematic deviations from the results of the Fujita–Mitazawa 3NF, but this deviation is not large and varies smoothly as a function of *N*. The difference between this 3NF and the Fujita–Mitazawa 3NF can then be remedied by shifting the value of the parameter $\Delta\varepsilon$ by −0.5 MeV, that is, from the present value of 0.82 MeV to 0.32 MeV (see the columns labelled 'Hebeler et al.−0.5*N*' in Extended Data Fig. 4). In other words, by using such a value of $\Delta\varepsilon$, one can probably describe the existence and structure of the nuclei of interest in a similar way to the present work, in terms of basically the same mechanism. We note that $c_\mathrm{D}$ and $c_\mathrm{E}$ are smaller in the delta-full formulation[58], where the excitation to the $\Delta$ particle is more explicitly included.

We now look at some individual terms in equation (1) coming from the 3NF. Although the $c_\mathrm{D}$ and $c_\mathrm{E}$ contact terms contribute, as a general property, to the rest (such as quadrupole) term, the actual contribution is quite small. For example, the expectation value of the rest term from the 3NF of Gazit et al.[80] remains 1.3 MeV for $^{34}$Mg to $^{40}$Mg with a decrease afterwards, whereas the total effect of this 3NF is of much larger magnitude, varying between −29 MeV and −26 MeV for $^{34}$Mg to $^{40}$Mg. Thus, the 3NF produces rather minor effects on the rest (such as quadrupole) term. On the other side, the 3NF effect on the monopole term is notable. We sketch how it occurs. Single-particle energies of valence nucleons are lowered by $\Delta$–hole excitations, but this lowering should be reduced by the Pauli blocking due to other valence nucleons. Such blocking effects can be incorporated by the monopole term of the Fujita–Mitazawa 3NF as described in ref. [23], and this effect is usually rather sizeable and general because of its origin. The dominance of the monopole effect over the other two terms in equation (1) is seen commonly in the 3NFs of Hebeler et al.[77] and Gazit et al.[80], resulting in cancellation of the total attractive monopole effect (20–30% in the case of Fig. 4).

Summarizing the discussions above, the *NN* interaction of the $\chi$EFT was renormalized in the present work by the $V_{\mathrm{low}k}$ calculation[54,55] with the cutoff parameter $\Lambda_{V\mathrm{low}k}$. The effects of the effective *NN* interaction for the configuration-interaction calculation are shown to be insensitive to this parameter around the present value, up to three decomposed components: monopole, pairing and rest. The 3NF affects mostly the monopole term of this effective *NN* interaction, and its effects are quite similar among the different 3NF options, or can be made so by a simple tuning. From these findings, the dripline mechanism proposed in this work appears to be natural and robust with respect to the variations of *NN* interactions.

The background of the features shown above with the case studies may be discussed as follows. First, as far as the ground and low-lying states are concerned, the low-momentum part of the effective *NN* interaction is more relevant than the high-momentum part. This feature is further strengthened for long-wavelength phenomena such as the shell structure and the shape evolution, which we focus on in this work. Second, all reasonable 'recipes' of the renormalization[54,55,82,83] probably lead to effective *NN* interactions with similar low-momentum properties, which is a natural consequence of the guiding principle for deriving the effective *NN* interaction: low-momentum properties of the original interaction must be reproduced. Third, because the EEdf1 interaction explains experiments rather well for low-energy and/or long-wavelength phenomena, we expect little room for substantial improvement by changing interactions. We thus expect that the present description of the interplay between the monopole and the rest effects by the EEdf1 interaction is close to the ultimate picture of the dripline, which can be shared by other ab initio effective *NN* interactions. This is also because the EEdf1 interaction was derived from one of the most frequently adopted nuclear forces in free space[22,53].

### Configuration-interaction calculation or shell-model calculation

The shell-model calculation is one of the standard methods in the nuclear many-body problem. It is similar to the configuration-interaction calculation in other fields of science. The single-particle orbits are defined first, on top of the inert core (or closed shell) (Fig. 1a). Protons and neutrons are put into these orbits. They are called valence protons or neutrons. Slater determinants are composed of single-particle states of these valence nucleons. We can construct the Hilbert space spanned by such Slater determinants. The matrix element of the Hamiltonian is calculated for each pair of the Slater determinants. Once all matrix elements are calculated, the matrix is diagonalized, to solve the Schrödinger equation. We then obtain energy eigenvalues of this Hamiltonian as well as their wavefunctions, from which we can calculate various physical quantities. This is an outline of the conventional shell-model calculation.

The number of such Slater determinants is called the shell-model dimension, and is crucial for the feasibility of actual computation. The maximum number of dimensions for which the conventional shell-model calculation can be performed is about $10^{11}$ at present[33]. Although this number of dimensions has been increased on average by a factor of two every two years, there are a number of highly interesting or important projects beyond this limit. In fact, the maximum shell-model dimension in the present work is $7.45 \times 10^{11}$ for $^{36}$Mg, which is well above the current limit stated above. The MCSM was introduced to overcome this difficulty[34,35], and is explained in the Methods. The shell-model interaction is also being studied for lighter nuclei in ab initio frameworks, for instance[70,72–74].

### Island of inversion

The island of inversion stands for the nine nuclei of $Z = 10$–$12$ and $N = 20$–$22$ in the Segrè chart. Although this terminology was introduced in ref. [12], the corresponding phenomena had earlier been recognized widely, as reviewed in refs. [13,27]. The island of inversion has served as a useful concept since then, in shell-model (configuration-interaction) calculations (for example, refs. [12,13,27,45,84–86], in comparison to a large number of experiments, such as in refs. [87–94]).

Because $N = 20$ is one of the magic numbers, the natural expectation is a neutron closed-shell ground state with a spherical shape (Fig. 1a, c). Intruder states with deformed shapes may then be found among excited states. In the picture of the island of inversion, however, an intruder state gains a large binding energy and becomes the ground state. This extra binding energy is due to a strong ellipsoidal deformation (Fig. 1e). If the closed shell structure remains (Fig. 1a), such strong deformation does not occur. On the other hand, particle–hole excitations across the $N = 20$ magic gap (Fig. 1b) can generally lead to strong deformation by creating or increasing valence particles in the *pf* shell and holes in the *sd* shell, as shown in Fig. 1b. Thus, the deformation and the particle–hole excitation are linked in the island of inversion. In the original picture of the island of inversion[12], the inversion occurs also for $N = 21$ and 22, but not for $N > 22$. The contribution from protons is also needed for a strong deformation: the deformation can be stronger for $Z = 10$–$12$, owing to particular occupations of proton single-particle orbits. Thus, the island of inversion picture suggests that the intruder ground states (that is, the 'inversion' phenomenon) emerge in the designated area of the Segrè chart, and that the nuclei outside the island of inversion are 'normal', having spherical ground states and retaining the $N = 20$ magic number.

The ellipsoidal deformation is a general phenomenon in atomic nuclei[7–9], and is not necessarily connected to particle–hole excitations across some magic gap. On the other side, a strong deformation can result in substantial particle–hole excitations over a magic gap, as a matter of the balance between the strength of the deformation and the size of the magic gap. In this sense, the mechanism of the island of inversion is a part of the general view of the nuclear deformation.

The island of inversion picture limits the nuclei with the 'inversion' to the nine nuclei mentioned above. This has been extensively studied; see recent reviews[13,27] for instance. It has been shown, however, in ref. [4], where the same framework was taken as the present work, that substantial particle–hole excitations occur in the ground states of relevant isotopes with $N < 20$, contrary to the island of inversion picture of ref. [12]. This is partly due to the shell evolution, meaning that the magic gap at $N = 20$ becomes smaller as a function of $Z$ (ref. [27]). The question then arises as to what happens in the nuclei with $N > 22$. This work shows the results up to the driplines, and as we show, the $N = 20$ closed-shell structure is kept broken all the way. The strong deformation persists up to the dripline, while the degree of the deformation varies.

### Monte Carlo shell model

The MCSM[34,35] uses Slater determinants as the basis vectors, similarly to the conventional shell-model calculation. However, the Slater determinants are not the same as those used in the conventional one. A basis vector for the MCSM calculation is a Slater determinant composed of 'stochastically and variationally' deformed single-particle states: Each such single-particle state is given by a certain superposition of the original single-particle states with amplitudes determined by stochastic and variational methods. By having some MCSM basis vectors produced and selected in this way, we diagonalize the Hamiltonian, and obtain energy eigenvalues and their wavefunctions.

These MCSM basis vectors are obtained one by one so that the energy eigenvalue of the state of interest is lowered sufficiently by adding a new one. For each MCSM basis vector, the single-particle amplitudes mentioned above need to be determined properly. They are searched by the stochastic process and are improved in the variational way. Because of the superposition over all single-particle states, the symmetries of the configuration-interaction Hamiltonian are lost, and the projection onto the angular momentum, the parity, and so on is carried out for the MCSM basis vector, already in the selection process of the basis vectors. Many candidates of such Slater determinant are tried and abandoned, keeping only those making sufficient contributions. Although there are a number of methodological refinements practically, we do not mention them here. Usually, we keep 50–100 MCSM basis vectors thus selected and polished. Since the computation can be quite large, the world's largest supercomputers, such as the K-computer (https://www.r-ccs.riken.jp/en/k-computer/about/), have been used.

### Decomposition of the interaction

A given effective *NN* interaction, $\upsilon_{NN}$, scatters a pair of nucleons in single-particle orbits $j_1$ and $j_2$ into a pair of single-particle orbits $j_3$ and $j_4$, conserving their total angular momentum $J$ and parity $\pi$. The isospin $T$ is relevant also, but is omitted here. This process is expressed by the so-called two-body matrix element

$$\langle j_3, j_4\ ; J^{\pi}\, | \upsilon_{NN} | j_1, j_2\ ; J^{\pi} \rangle. \tag{2}$$

The monopole interaction[13,27], $\upsilon_{\mathrm{mono}}$ in equation (1), is defined as an interaction with a constant strength (coupling constant) common to any pair of a nucleon in orbit $j_1$ and the other nucleon in orbit $j_2$. This constant strength should reproduce the average effect of $\upsilon_{NN}$ for the orbits $j_1$ and $j_2$, and hence is given by the monopole matrix element

$$V^{m}(j_1, j_2) = \frac{\sum_J (2J+1) \langle j_1, j_2\ ; J^{\pi}\, | \upsilon_{NN} | j_1, j_2\ ; J^{\pi} \rangle}{\sum_J (2J+1)}, \tag{3}$$

where $J$ in the summation takes all possible values with certain limitations due to the Pauli principle for the cases with $j_1 = j_2$ (same orbit). The monopole matrix element is indeed the average over all possible orientations when a nucleon is in the orbit $j_1$ and the other in the orbit $j_2$. The monopole interaction keeps quantum states of these two nucleons. The strength varies in general if $j_1$ or $j_2$ is changed. It is analogous to the bond between two quantum objects (like atoms), in the sense that only average effects are carried (without fine details). A more precise and pedagogical explanation, including isospin properties, can be found in a review article[27]. We point out once again that the monopole interaction is uniquely determined from a given effective *NN* interaction.

The pairing interaction, $\upsilon_{\mathrm{pair}}$, is represented by the two-body matrix elements

$$\langle j_3, j_3\ ; J^{\pi} = 0^{+} | \upsilon_{NN} - \upsilon_{mono} | j_1, j_1\ ; J^{\pi} = 0^{+} \rangle. \tag{4}$$

We consider the pairing interaction between neutrons and the pairing interaction between protons, whereas the one between a proton and a neutron is not considered in this work. The pairing interaction then represents an interaction acting on two identical fermions in time-reversal states, which is analogous to the BCS pairing of electrons in condensed matter. To avoid double counting, the monopole-interaction component is subtracted from $v_{NN}$ in equation (4), but this is a minor point because of the $(2J+1)$ factor in equation (3) and $J=0$ for the pairing. In fact, the contribution of the monopole component of the pairing interaction, which is included not in the pairing segment but in the monopole segment in Fig. 4, is small (less than about 2 MeV) and does not change rapidly as a function of the neutron number. We point out that the pairing interaction favours states of spherical shapes.

The rest interaction is given by:

$$v_{\rm rest} = v_{NN} - v_{\rm mono} - v_{\rm pair} \tag{5}$$

As mentioned in the main text, $v_{\rm rest}$ contains many terms, but the most dominant one in the present issue is the quadrupole–quadrupole interaction, for which the main contribution comes from the coupling between the proton quadrupole operator and the neutron quadrupole operator. Because of the construction, three terms, $v_{\rm mono}$, $v_{\rm pair}$ and $v_{\rm rest}$, exclude each other, and their total sum constitutes the interaction $v_{NN}$.

## Data availability

All data relevant to this study are shown in the paper, but if more details are needed, they are available from the corresponding author upon reasonable request.

## Code availability

Several codes for the conventional shell-model (configuration-interaction) calculation are available, of which we used KSHELL[33] in the present work. Reasonable inquiries about the MCSM code will be responded to by the corresponding author.

51. Hjorth-Jensen, M., Kuo, T. T. S. & Osnes, E. Realistic effective interactions for nuclear systems. *Phys. Rep*. **261**, 125–270 (1995).
52. Krenciglowa, E. M. & Kuo, T. T. S. Convergence of effective Hamiltonian expansion and partial summations of folded diagrams. *Nucl. Phys. A* **235**, 171–189 (1974).
53. Entem, D. R. & Machleidt, R. Accurate charge-dependent nucleon-nucleon potential at fourth order of chiral perturbation theory. *Phys. Rev. C* **68**, 041001 (2003).
54. Bogner, S., Kuo, T. T. S., Coraggio, L., Covello, A. & Itaco, N. Low momentum nucleon-nucleon potential and shell model effective interactions. *Phys. Rev. C* **65**, 051301 (2002).
55. Nogga, A., Bogner, S. K. & Schwenk, A. Low-momentum interaction in few-nucleon systems. *Phys. Rev. C* **70**, 061002 (2004).
56. Carlson, J. et al. Quantum Monte Carlo methods for nuclear physics. *Rev. Mod. Phys*. **87**, 1067 (2015).
57. Pastore, S. et al. Quantum Monte Carlo calculations of weak transitions in $A$ = 6–10 nuclei. *Phys. Rev. C* **97**, 022501 (2018).
58. Ekström, A., Hagen, G., Morris, T. D., Papenbrock, T. & Schwartz, P. D. Δ isobars and nuclear saturation. *Phys. Rev. C* **97**, 024332 (2018).
59. Honma, M., Otsuka, T., Brown, B. A. & Mizusaki, T. Effective interaction for *pf*-shell nuclei. *Phys. Rev. C* **65**, 061301 (2002).
60. Notani, M. et al. New neutron-rich isotopes, $^{34}$Ne, $^{37}$Na and $^{43}$Si, produced by fragmentation of a 64 A MeV $^{48}$Ca beam. *Phys. Lett. B* **542**, 49–54 (2002).
61. Baumann, T. et al. Discovery of $^{40}$Mg and $^{42}$Al suggests neutron drip-line slant towards heavier isotopes. *Nature* **449**, 1022–1024 (2007).
62. Hagen, G. et al. Neutron and weak-charge distributions of the $^{48}$Ca nucleus, estimated uncertainties from truncations of employed method and model space. *Nat. Phys*. **12**, 186–190 (2016).
63. Hergert, H., Binder, S., Calci, A., Langhammer, J. & Roth, R. *Ab initio* calculations of even oxygen isotopes with chiral two-plus-three-nucleon interactions. *Phys. Rev. Lett*. **110**, 242501 (2013).
64. Hergert, H. et al. *Ab initio* multireference in-medium similarity renormalization group calculations of even calcium and nickel isotopes. *Phys. Rev. C* **90**, 041302 (2014).
65. Stroberg, S. R., Hergert, H., Bogner, S. K. & Holt, J. D. Nonempirical interactions for the nuclear shell model: an update. *Annu. Rev. Nucl. Part. Sci*. **69**, 307–362 (2019).
66. Simonis, J., Hebeler, K., Holt, J. D., Menendez, J. & Schwenk, A. Exploring *sd*-shell nuclei from two- and three-nucleon interactions with realistic saturation properties. *Phys. Rev. C* **93**, 011302 (2016).
67. Morris, T. D. et al. Structure of the lightest tin isotopes. *Phys. Rev. Lett*. **120**, 152503 (2018).
68. Holt, J. D., Menendez, J., Simonis, J. & Schwenk, A. Three-nucleon forces and spectroscopy of neutron-rich calcium isotopes. *Phys. Rev. C* **90**, 024312 (2014).
69. Smirnova, N. A. et al. Effective interactions in the *sd* shell. *Phys. Rev. C* **100**, 054329 (2019).
70. Dikmen, E. et al. Ab initio effective interactions for *sd*-shell valence nucleons. *Phys. Rev. C* **91**, 064301 (2015).
71. Hergert, H., Bogner, S. K., Morris, T. D., Schwenk, A. & Tsukiyama, K. The in-medium similarity renormalization group: a novel *ab initio* method for nuclei. *Phys. Rep*. **621**, 165–222 (2016).
72. Epelbaum, E., Hammer, H.-W. & Meißner, Ulf-G. Modern theory of nuclear forces. *Rev. Mod. Phys*. **81**, 1773 (2009).
73. Bogner, S. K. et al. Nonperturbative shell-model interactions from the in-medium similarity renormalization group. *Phys. Rev. Lett*. **113**, 142501 (2014).
74. Jansen, G. R., Engel, J., Hagen, G., Navratil, P. & Signoracci, A. Ab initio coupled-cluster effective interactions for the shell model: application to neutron-rich oxygen and carbon isotopes. *Phys. Rev. Lett*. **113**, 142502 (2014).
75. Stroberg, S. R., Hergert, H., Holt, J. D., Bogner, S. K. & Schwenk. A. Ground and excited states of doubly open-shell nuclei from ab initio valence-space Hamiltonians. *Phys. Rev. C* **93**, 051301(R) (2016).
76. Coraggio, L., Gargano, A. & Itaco, N. Double-step truncation procedure for large-scale shell-model calculations. *Phys. Rev. C* **93**, 064328 (2016).
77. Hebeler, K., Bogner, S. K., Furnstahl, R. J., Nogga, A. & Schwenk, A. Improved nuclear matter calculations from chiral low-momentum interactions. *Phys. Rev. C* **83**, 031301 (2011).
78. van Kolck, U. Few-nucleon forces from chiral Lagrangians. *Phys. Rev. C* **49**, 2932 (1994).
79. Epelbaum, E. et al. Three-nucleon forces from chiral effective field theory. *Phys. Rev. C* **66**, 064001 (2002).
80. Gazit, D., Quaglioni, S. & Navrátil, P. Three-nucleon low-energy constants from the consistency of interactions and currents in chiral effective field theory. *Phys. Rev. Lett*. **103**, 102502 (2009); erratum **122**, 029901 (2019).
81. Kohno, M. Nuclear and neutron matter G-matrix calculations with a chiral effective field theory potential including effects of three-nucleon interactions. *Phys. Rev. C* **88**, 064005 (2013); erratum **96**, 059903 (2017).
82. Bogner, S. K., Furnstahl, R. J. & Perry, R. J. Similarity renormalization group for nucleon-nucleon interactions. *Phys. Rev. C* **75**, 061001(R) (2007).
83. Bogner, S. K., Furnstahl, R. J., Ramanan, S. & Schwenk, A. Low-momentum interactions with smooth cutoffs. *Nucl. Phys. A* **784**, 79–103 (2007).
84. Wildenthal, B. H. & Chung, W. Collapse of the conventional shell-model ordering in the very-neutron-rich isotopes of Na and Mg. *Phys. Rev. C* **22**, 2260 (1980).
85. Watt, A., Singhal, R. P., Storm, M. H. & Whitehead, R. R. A shell-model investigation of the binding energies of some exotic isotopes of sodium and magnesium. *J. Phys. G* **7**, L145–L148 (1981).
86. Utsuno, Y., Otsuka, T., Mizusaki, T. & Honma, M. Varying shell gap and deformation in $N \sim 20$ unstable nuclei studied by the Monte Carlo shell model. *Phys. Rev. C* **60**, 054315 (1999).
87. Motobayashi, T. et al. Large deformation of the very neutron-rich nucleus $^{32}$Mg from intermediate-energy Coulomb excitation. *Phys. Lett. B* **346**, 9–14 (1995).
88. Gade, A. et al. Spectroscopy of $^{36}$Mg: interplay of normal and intruder configurations at the neutron-rich boundary of the "island of inversion". *Phys. Rev. Lett*. **99**, 072502 (2007).
89. Doornenbal, P. et al. Spectroscopy of $^{32}$Ne and the "island of inversion". *Phys. Rev. Lett*. **103**, 032501 (2009).
90. Nakamura, T. et al. Halo structure of the island of inversion nucleus $^{31}$Ne. *Phys. Rev. Lett*. **103**, 262501 (2009).
91. Doornenbal, P. et al. In-beam γ-ray spectroscopy of $^{34,36,38}$Mg: merging the $N$ = 20 and $N$ = 28 shell quenching. *Phys. Rev. Lett*. **111**, 212502 (2013).
92. Kobayashi, N. et al. Observation of a *p*-wave one-neutron halo configuration in $^{37}$Mg. *Phys. Rev. Lett*. **112**, 242501 (2014).
93. Crawford, H. L. et al. Rotational band structure in $^{32}$Mg. *Phys. Rev. C* **93**, 031303(R) (2016).
94. Doornenbal, P. et al. Low-$Z$ shore of the "island of inversion" and the reduced neutron magicity toward $^{28}$O. *Phys. Rev. C* **95**, 041301(R) (2017).

**Acknowledgements** N.T., T.O. and N.S. acknowledge partial support from MEXT via the "Priority Issue on post-K computer" (Elucidation of the Fundamental Laws and Evolution of the Universe) grants (hp160211, hp170230, hp180179, hp190160), partial support from MEXT via the "Program for Promoting Researches on the Supercomputer Fugaku" (Simulation for basic science: from fundamental laws of particles to creation of nuclei) grant (hp200130) and from Joint Institute for Computational Fundamental Science (JICFuS). This work was supported in part by JSPS KAKENHI grant JP19H05145. N.S. and T.S. acknowledge JSPS KAKENHI grants JP17K05433 and JP19K03855, respectively. T.O. thanks P. Van Duppen for valuable comments and Y. Aritomo and H. Koura for information. We thank T. Abe and Y. Tsunoda for help. N.T., T.O. and K.T. are grateful to M. H.-Jensen for collaboration.

**Author contributions** N.T. derived the EEdf1 interaction and performed many of the configuration-interaction calculations; T.O. supervised the whole study; K.T. derived the EKK method and contributed to in-depth discussions; N.S. wrote most of the computer codes and performed some calculations; T.S. calculated the Fujita–Miyazawa three-nucleon interaction; Y.U. contributed to detailed discussions; S.Y. calculated the χEFT three-nucleon interactions, H.U. suggested this project at the initial stage; and T.O. wrote the manuscript. All authors discussed the results and commented on the manuscript.

**Competing interests** The authors declare no competing interests.

**Additional information**

**Correspondence and requests for materials** should be addressed to T.O.

**Peer review information** *Nature* thanks Calvin Johnson and the other, anonymous, reviewer(s) for their contribution to the peer review of this work.

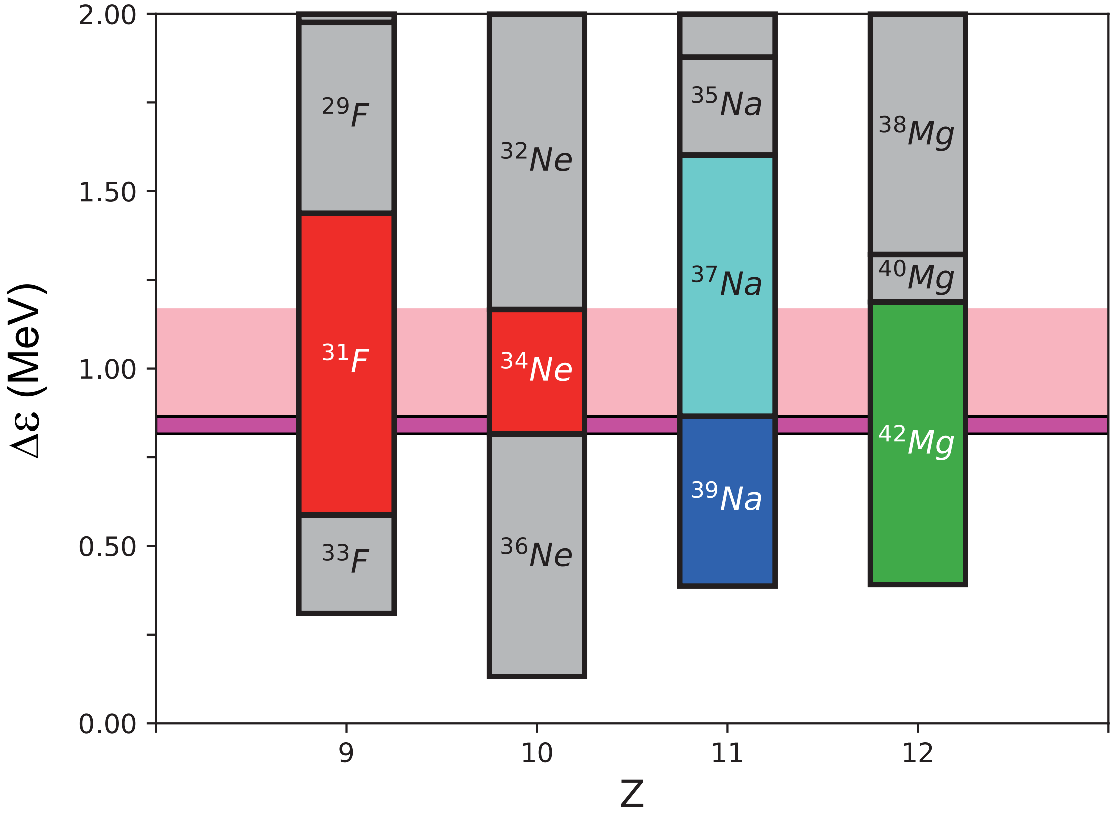

**Extended Data Fig. 1 | Dripline nucleus in each chain of isotopes as a function of Δ*ε*.** The single-particle energies are shifted from their original values by the same amount, Δ*ε*, which is the vertical axis. The dark pink belt indicates the range of Δ*ε* suggested by the recent experiment[39] identifying $^{31}$F, $^{34}$Ne and $^{39}$Na as dripline nuclei, while the light pink belt is obtained similarly but by assuming $^{37}$Na is the dripline nucleus of Na isotopes.

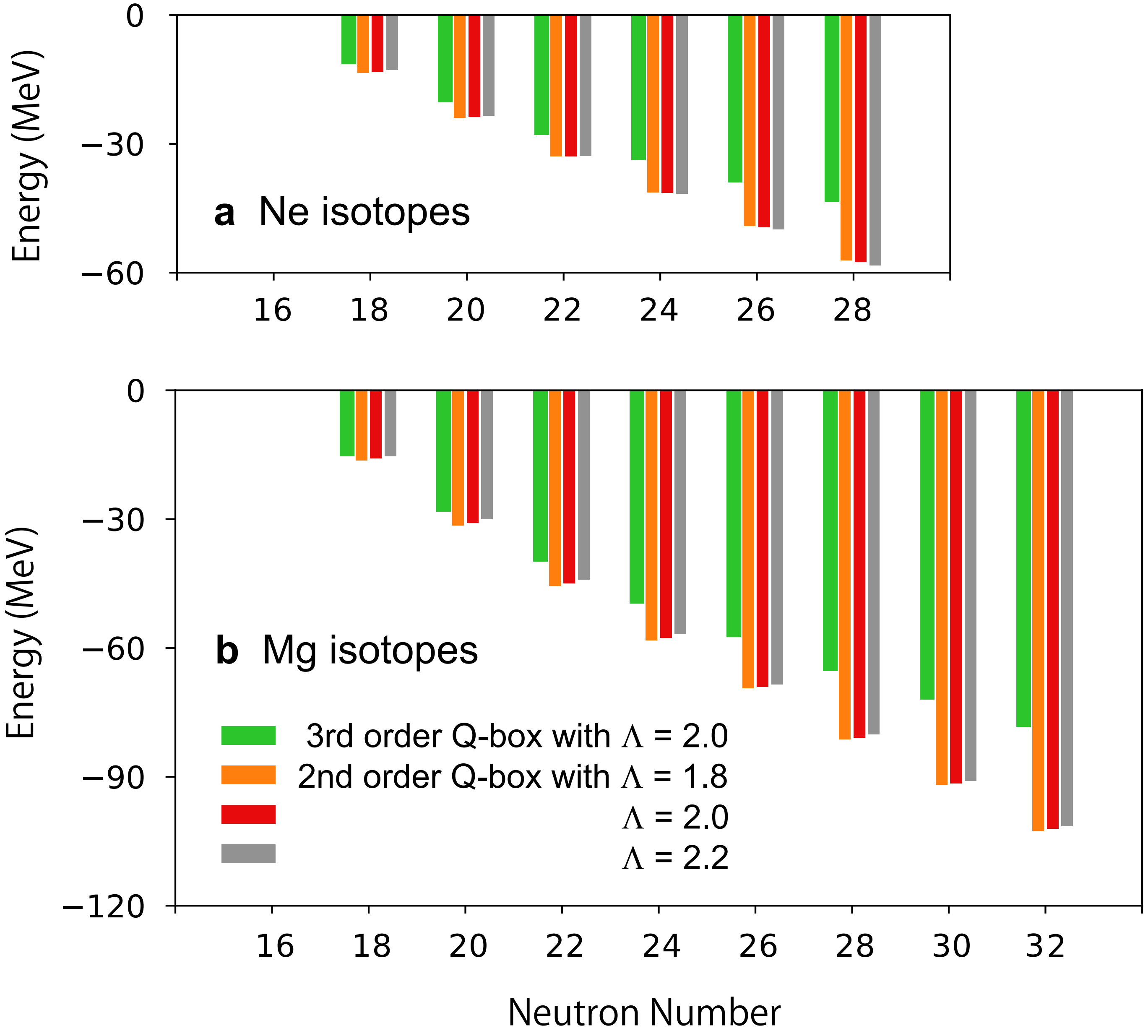

**Extended Data Fig. 2 | Dependences of the ground-state energy on the cutoff parameter of the $V_{\mathrm{lowk}}$ approach.** The ground-state expectation value of the effective *NN* interaction originating in the $\chi$EFT *NN* forces by Entem and Machleidt[22,53] (Methods) are shown for the Ne and Mg isotopes. **a**, Ne; **b**, Mg. For each isotope, the second (orange), third (red) and fourth (grey) columns depict, respectively, this quantity obtained with the cutoff parameter $\Lambda_{V\mathrm{lowk}} = 1.8\,\mathrm{fm}^{-1}$, $2.0\,\mathrm{fm}^{-1}$ and $2.2\,\mathrm{fm}^{-1}$ by the second-order $\hat{Q}$-box calculation in the EKK process. For comparison, the third-order $\hat{Q}$-box result with $\Lambda_{V\mathrm{lowk}} = 2.0\,\mathrm{fm}^{-1}$ is shown by the first (green) column. All values are shown relative to their corresponding $N = 16$ values.

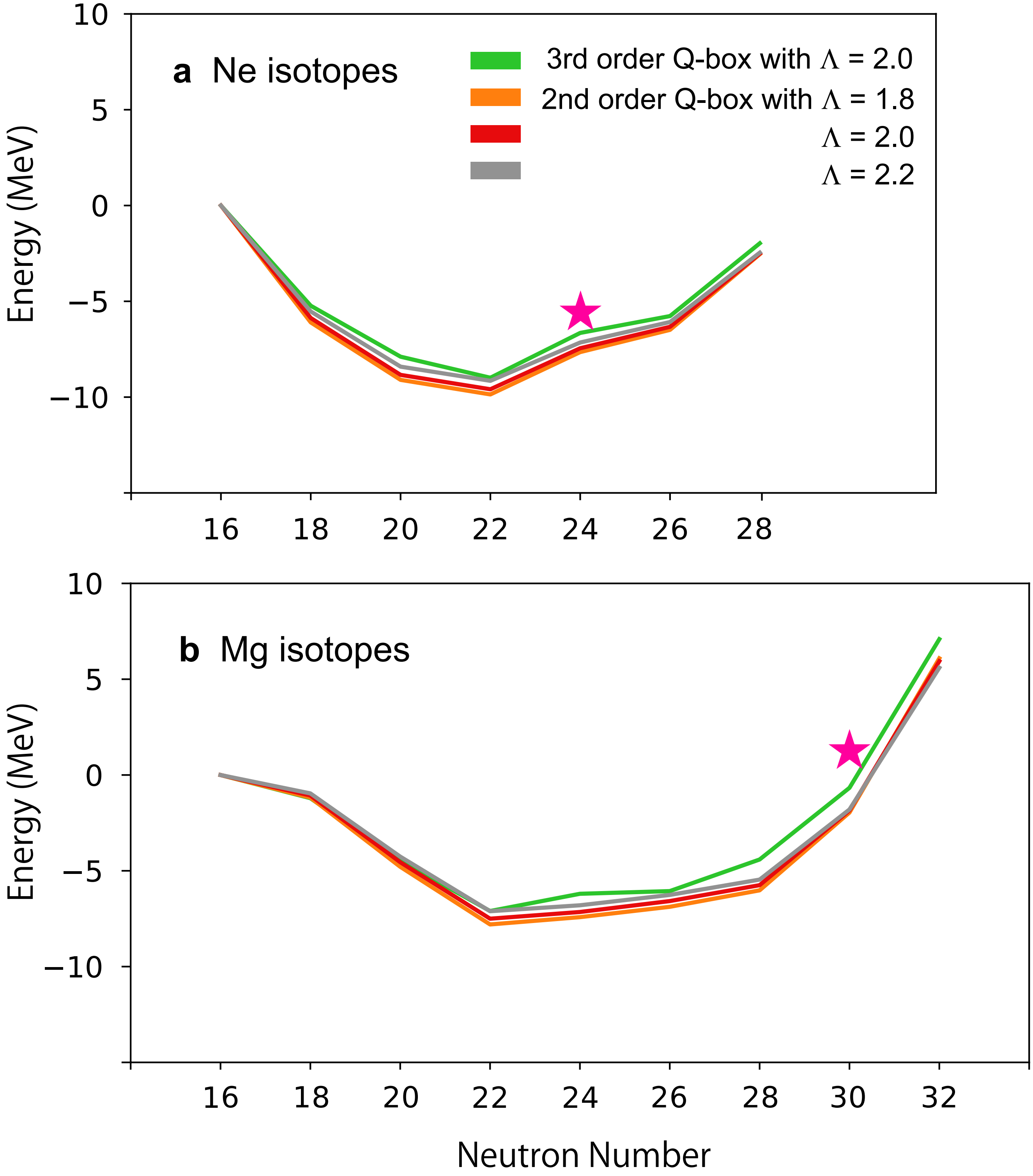

**Extended Data Fig. 3 | Dependences of the rest interaction contribution on the cutoff parameter of the $V_{\mathrm{lowk}}$ approach.** Cutoff dependences of the ground-state expectation value of the rest (such as quadrupole) term of the effective *NN* interaction originating in the $\chi$EFT *NN* forces by Entem and Machleidt[22,53] (Methods) are shown for the Ne and Mg isotopes. **a**, Ne; **b**, Mg. For each isotope, the orange, red and grey lines depict, respectively, this quantity obtained with the cutoff parameter $\Lambda_{Vlowk}$ = 1.8 fm$^{-1}$, 2.0 fm$^{-1}$ and 2.2 fm$^{-1}$ by the second-order $\hat{Q}$-box calculation in the EKK process. For comparison, the third-order $\hat{Q}$-box result with $\Lambda_{Vlowk}$ = 2.0 fm$^{-1}$ is shown by the green line. All values are shown relative to their corresponding $N$ = 16 values. The dripline isotopes suggested by the present work are indicated by star symbols.

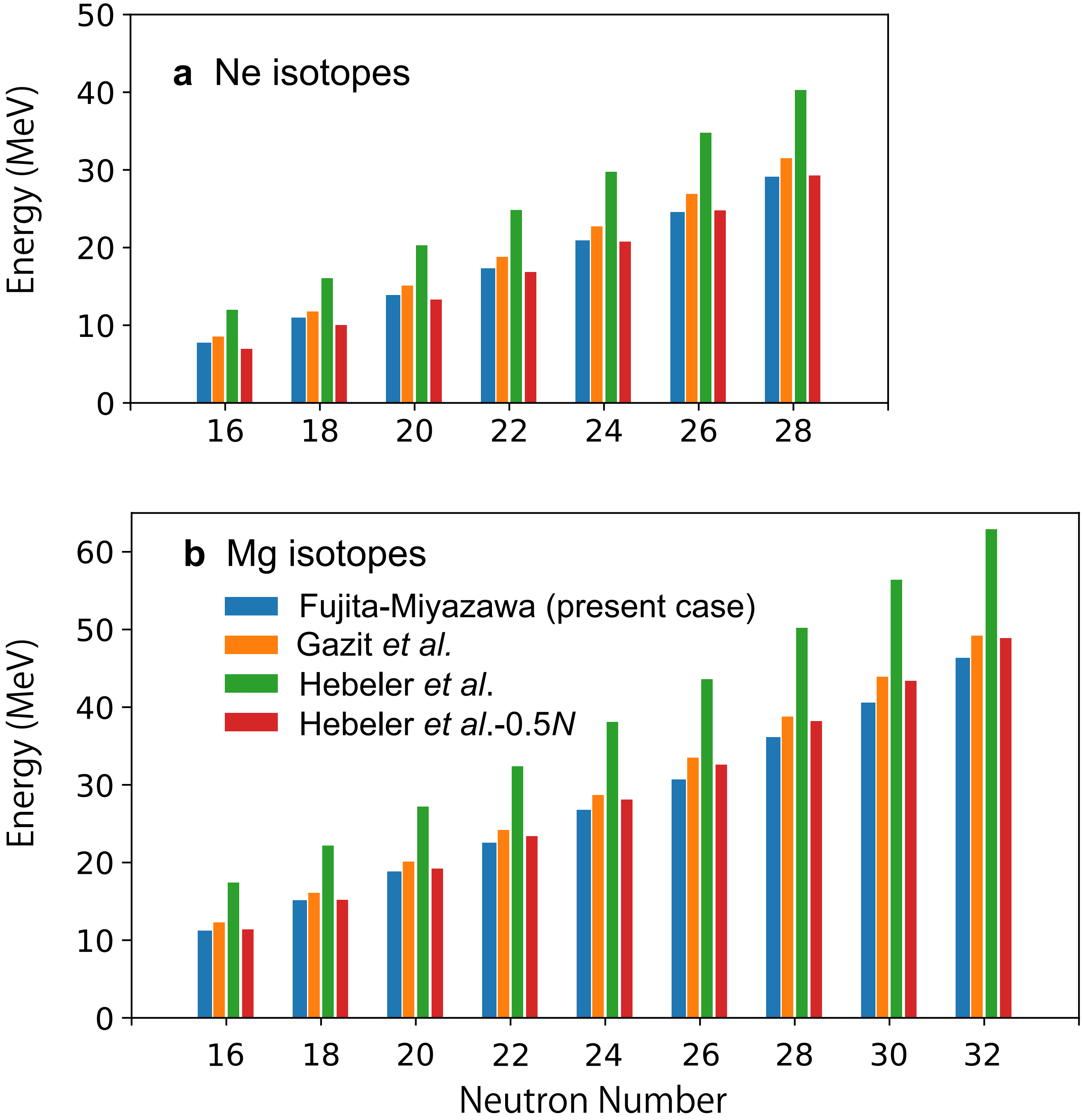

**Extended Data Fig. 4 | Ground-state expectation value of the 3NF for the Ne and Mg isotopes.** **a**, Ne; **b**, Mg. For each isotope, the second (orange), third (green) and fourth (red) columns depict, respectively, this quantity obtained with the 3NF of Gazit et al.[80], that of Hebeler et al.[77] and that of Hebeler et al. with single-particle energy shift (labelled 'Hebeler et al.−0.5*N*') (Methods). For comparison, the same quantity by the Fujita–Miyazawa 3NF is shown by the first (blue) column.